AGU100 ADVANCING EARTH AND SPACE SCIENCE

Geophysical Research Letters

RESEARCH LETTER
10.1029/2019GL083093

Earthquakes Within Earthquakes: Patterns in Rupture Complexity

Philippe Danré[1,2], Jiuxun Yin[1], Bradley P. Lipovsky[1], and Marine A. Denolle[1]

[1]Department of Earth and Planetary Sciences, Harvard University, Cambridge, MA, USA, [2]Département de Géosciences, École Normale Supérieure, PSL Research University, Paris, France

Key Points:
- Earthquake source time functions are composed of subevents
- The number of subevents grows with the total earthquake moment, and subevent moments scale with main event moments
- Source time function complexity can be explained by self-affine prestress heterogeneity

Supporting Information:
- Supporting Information S1

Correspondence to:
M. A. Denolle,
mdenolle@fas.harvard.edu

Citation:
Danré, P., Yin, J., Lipovsky, B. P., & Denolle, M. A. (2019). Earthquakes within earthquakes: Patterns in rupture complexity. *Geophysical Research Letters*, *46*, 7352–7360. https://doi.org/10.1029/2019GL083093

Received 1 APR 2019
Accepted 18 JUN 2019
Accepted article online 25 JUN 2019
Published online 8 JUL 2019

Abstract Earthquake source time functions carry information about the complexity of seismic rupture. We explore databases of earthquake source time functions and find that they are composed of distinct peaks that we call subevents. We observe that earthquake complexity, as represented by the number of subevents, grows with earthquake magnitude. Patterns in rupture complexity arise from a scaling between subevent moment and main event moment. These results can be explained by simple 2-D dynamic rupture simulations with self-affine heterogeneity in fault prestress. Applying this to early magnitude estimates, we show that the main event magnitude can be estimated after observing only the first few subevents.

Plain Language Summary Seismograms are measurements of waves from earthquakes. They give us information about what happened on the fault at the place where the earthquake occurred. Seismograms can be difficult to interpret because they are often very complicated. Why? One reason is that the waves change when they travel long distances between the fault and a seismometer. Seismologists correct for this effect, however, by constructing something called a source time function. Source time functions are much easier to understand than raw seismograms. We examine a catalog of source time functions from around the world. We find that large earthquakes are composed of many smaller events that we call subevents. The size of a subevent is related to the size of the main earthquake. One important outcome is that we can predict the final size of an earthquake after observing only the first few subevents.

1. Introduction

Whether earthquake complexity reflects underlying organization or randomness is a fundamental issue in earthquake physics and predictability. Recent work has suggested that organization in earthquake complexity permits a sense of determinism whereby observations made in a short period of time at the beginning of an earthquake may be used to infer the overall event size and style (Olson & Allen, 2005; Melgar & Hayes, 2017; Goldberg et al., 2018; Allen & Melgar, 2019). Previous studies have found that early *P* wave arrivals carry information about the overall earthquake size (Iio, 1995; Beroza & Ellsworth, 1996; Allen & Kanamori, 2003; Olson & Allen, 2005), but such correlations bear large uncertainties that necessitate additional information, such as attenuation parameters, in order to conduct meaningful early magnitude estimation (Wu et al., 2006; Colombelli et al., 2014; Noda & Ellsworth, 2016). The direct *P* wave arrival, however, represents only a small fraction of the available and potentially deterministic information (Vallée et al., 2017; Vallée & Juhel, 2019).

The seismic signature of earthquake processes is captured in the Source Time Function (STF). Conventional approaches to estimating the STF fall into two categories. The first inverts for a kinematic evolution of slip on the fault from recorded body and surface waves and yields the moment rate function (Hayes, 2017; Ji et al., 2002; Kikuchi & Kanamori, 1991; Ye et al., 2016). Due to data resolution, this approach works best for large earthquakes; published databases have few examples. The second approach makes a point source approximation to the rupture and directly deconvolves recorded seismic waves with a Green's function (Mueller, 1985; Tanioka & Ruff, 1997; Vallée & Douet, 2016). This second method assumes that the far-field pulse is proportional to the moment rate function when averaged over stations, is appropriate for small to moderate earthquakes, and results in larger ensembles of STFs.

Here, we take advantage of existing STF catalogs in order to explore earthquake complexity. The main result of this paper is that larger earthquakes are more complex—on average—than smaller ones. We find that

earthquake complexity grows with earthquake size in a structured manner. To our knowledge, no previous study has found systematic growth in complexity with earthquake size (Boatwright, 1984; Houston et al., 1998; Houston, 2001; Meier et al., 2017; Stork & Ito, 2004). The main reason why our results differ from these previous studies is probably that we use much larger catalogs. As a result, we find that inherent structure in earthquake complexity can be used to infer a likely final earthquake size in the first few seconds of large earthquakes.

2. Methods

2.1. Data

The SCARDEC (Seismic source ChActeristics Retrieved from DEConvolvolving teleseismic body waves, Vallée and Douet (2016), http://scardec.projects.sismo.ipgp.fr/, last accessed 11 November 2018) database contains 3,395 STFs for earthquakes with magnitude from $M5.5$ to $M9.0$ between 1992 and 2017. The SCARDEC functions are constructed from the deconvolution of teleseismic P waves (P, pP, sP, PP, and PcP) with a theoretical Green's function that is estimated from a radially symmetric and anelastic Earth. Because the global models of attenuation are better constrained by seismic frequencies lower than 1 Hz, we do not interpret signals that are shorter than 1 s in the following analysis. The United States Geological Survey (USGS) STF database (Hayes, 2017) contains 180 events (as of 12 April 2018) of earthquakes of magnitude greater than 7 during the period 1990–2017. STFs in the USGS database are reconstructed from an inverted kinematic model that follows the algorithm developed by Ji et al. (2002) and that jointly inverts for body and surface waves. This latter data set serves as a validation set to our analysis of the SCARDEC database and has been shown to provide STFs comparable to the SCARDEC database by Meier et al. (2017). Both databases have been extensively studied to extract physical properties of earthquakes such as moment, duration, stress drop, radiated energy, and rupture velocity (Chounet et al., 2018; Chounet & Vallée, 2018; Denolle, 2019; Meier et al., 2017; Melgar & Hayes, 2017; Vallée, 2013; Vallée & Douet, 2016). The sampling rate of the SCARDEC database is $\mathrm{d}t = 0.0703$ s and we recalculate the USGS moment rate function to that sampling rate from the finite fault models and the slip rate bases described in Ji et al. (2002).

STFs have a basic structure consisting of an initial acceleration of seismic moment followed by a deceleration. When averaged over many events, STFs have maximum values around 30–50% of their duration (Denolle, 2019; Meier et al., 2017; Melgar & Hayes, 2017). Despite this first-order similarity in shapes, dissimilarity among STFs becomes obvious for large events (as discussed in Meier et al., 2017). In the following, we explore the roughness in the shape of the STF as a metric of earthquake complexity.

2.2. Numerical Simulations

We construct a database of synthetic STFs derived from dynamic rupture simulations. These simulations solve the equations of elastodynamics in two spatial dimensions (antiplane strain) with linear slip weakening friction acting along a one-dimensional fault. This coupled elasticity-friction problem is solved using the spectral boundary integral method (SBIEMLAB, code developed by Jean-Paul Ampuero, http://web.gps.caltech.edu/~ampuero/software.html, last accessed 27 November 2018). Although rupture complexity may arise from heterogeneity in prestress (Huang et al., 2012; Ripperger et al., 2007), geometry (Ando & Kaneko, 2018; Hamling et al., 2017), roughness (Dunham et al., 2011; Fang & Dunham, 2013), or fault strength (Ide & Aochi, 2005), the goal of the paper is not to explore this full parameter space, but rather test whether heterogeneity in prestress explains observed STF characteristics (presented below). The fault prestress is defined as having a spatially uniform mean value plus a spatially varying perturbation that follows a power law power spectral density $P_m(k) \sim k^{-\gamma}$, where k is the wave number and the exponent γ is chosen as 0.8. Additional details concerning the numerical simulations are discussed in the supporting information (see Text S3 and Figures S7 and S8).

We produce 600 prestress distributions and run dynamic ruptures by randomly selecting a nucleation location. We only keep the 499 of these where the rupture did not propagate beyond the zone of self-affine prestress. We generate earthquakes with over 2 orders of magnitude difference. For these simulated earthquakes we calculate STFs by integrating the moment rate (per unit fault width) over the fault dimension (see Figure S8). Because the simulated STF contains higher-frequency content than the data set of observed STFs, we smooth the simulated moment rate functions by convolving the simulated STF with a Gaussian of width $\sigma = 2$ s. We also attempted to use a Butterworth-type low-pass filter, but this resulted in nonphysical negative values of the moment rate function.

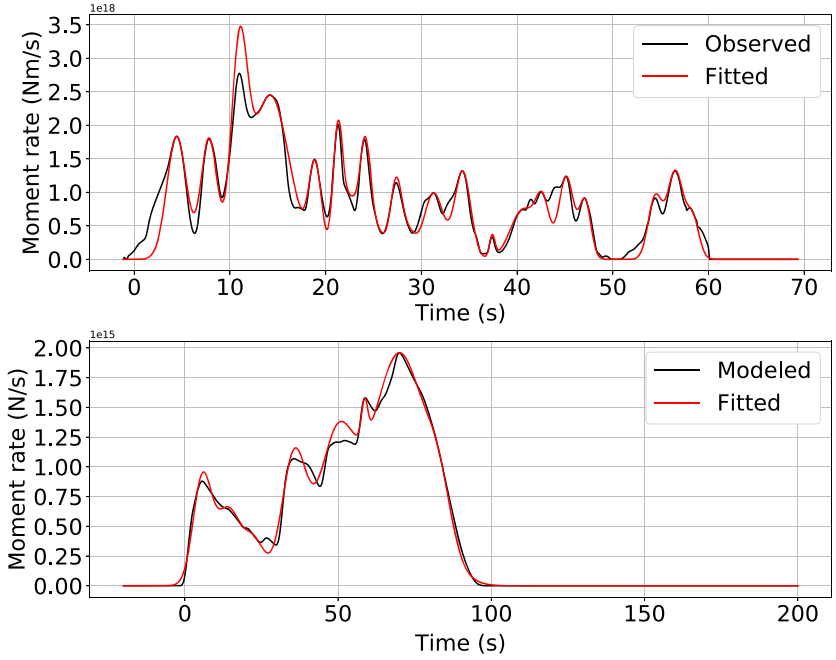

Figure 1. (top) Observed Source Time Function (STF) from the SCARDEC database from the 14 March 1994 *M*7.1 Central Mid-Atlantic Ridge Earthquake in black and the fitted Gaussian-built STF in red. (bottom) Modeled STF in moment rate per unit of fault width (black) and the corresponding fitted Gaussian-built STF (red). This illustrates the reliability of our fitting procedure in capturing the shape and moment of STFs. SCARDEC = Seismic source ChActeristics Retrieved from DEConvolvolving teleseismic body waves.

2.3. Subevent Decomposition

The roughness of both the observed and simulated STFs may be described in several ways. Several studies use the zero crossings of the moment acceleration function (Houston et al., 1998; Houston, 2001; Sato & Mori, 2006), while others use the log-residuals between the STF and a smoothed model (Meier et al., 2017). Here, we decompose the STF as a sum of "subevents" that are Gaussian pulses, similar to the pulse stripping method of Kikuchi and Kanamori (1982) and Zhan et al. (2014). Gaussian subevents were found to best fit the shape of the SCARDEC STFs (see Figures S5 and S6). We perform the subevent decomposition from onset of rupture (time zero) as follows:

1. go forward in time and detect a peak S_S (local maximum over three points or 0.21 s) at time t_S that satisfies $S_S > 0.1\,\max(\mathrm{STF})$;
2. fit a Gaussian function centered around t_S to the STF with an amplitude to S_S and a width σ estimated using a grid search minimizing the root-mean-square residuals (effectively to get a subevent duration and moment) over 11 grid points, or 0.77 s;
3. if $4\sigma > 1$ s, count the detection as subevent and move forward, otherwise go back to step 1;
4. subtract the fitted Gaussian function from the STF;
5. if more time remains in the STF, return to step 1.

We apply the same algorithm to all STFs (simulated and the observed SCARDEC and USGS). Examples of the reconstructed STFs are shown in Figure 1 for both the observed STF and the simulated STF. The choice of a threshold to select the peak based on the maximum amplitude of the STF, here 0.1, is necessary to ignore spurious residuals that are not resolvable by the data (e.g., for shorter duration or lower amplitude signals). Other thresholds resulted in detecting smaller subevents that we interpret as being overfit (Figure S2). This interpretation is based on the low likelihood of resolving small subevents given the depletion of high-frequency energy at teleseismic distances. Regardless of the threshold, the results presented below remained unchanged.

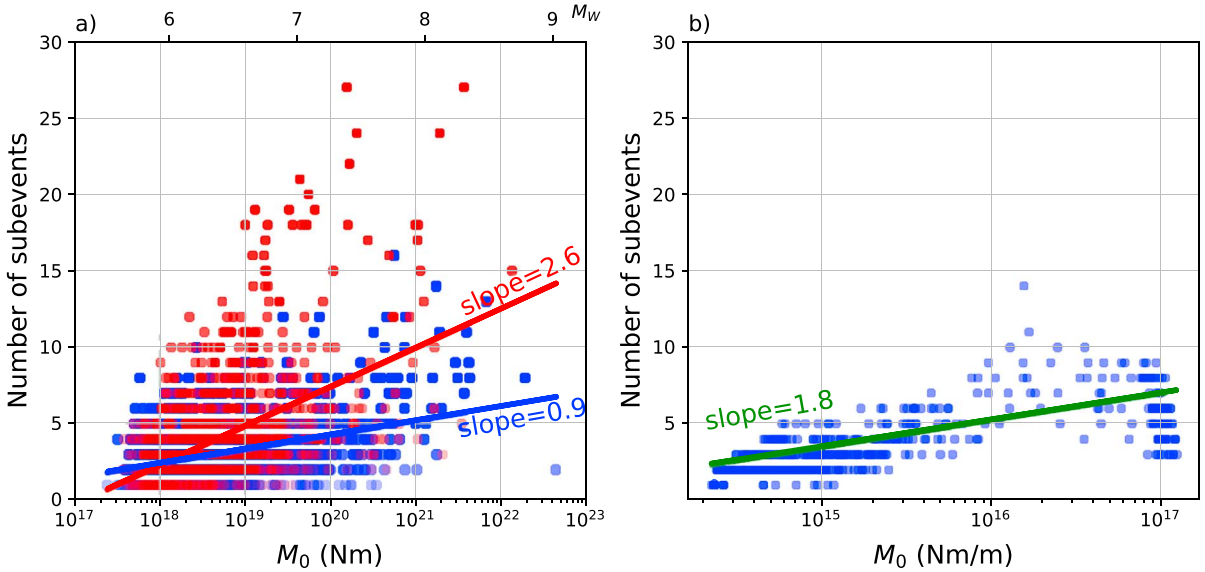

Figure 2. Number of subevents as a function of main event seismic moment for (a) the observed SCARDEC STFs and (b) the modeled STFs. Dots are the individual earthquakes. Dots are colored according to whether the faulting type parameter F_M defined in Shearer et al. (2006), which is between −0.5 and 0.5 for strike slip (red dots), and between −1 and −0.5 or 0.5 to 1 for dip slip (blue dots). The slopes that best explain the variance in a linear regression of both subsets are shown in colored letters. The growth in complexity is monotonic with earthquake size for the observations, except for the *M*9.0 2011 Tohoku earthquake, and the growth is noticeable for the simulations. SCARDEC = Seismic source ChActeristics Retrieved from DEConvolvolving teleseismic body waves; STF = Source Time Function.

3. Results

3.1. Earthquake Complexity

Using the number of subevents as a metric for earthquake complexity, we find our first main result: earthquake complexity increases with earthquake size (Figure 2a). In general, $M_0 < 4 \times 10^{19}$ (Nm) ($\sim M_W 7$) earthquakes have about 1–4 subevents (mean of 3.08), while the $M_0 > 4 \times 10^{19}$ earthquakes have 4–10 subevents (mean of 5.84). We find similar systematic growth in complexity using the smaller USGS database, as discussed in the supporting information (Figure S1a).

The growth in the number of observed subevents with earthquake magnitude is more pronounced for strike-slip earthquakes with magnitudes greater than $M_W \approx 6.75$ ($M_0 \geq 1.68 \times 10^{19}$ Nm) as the slope is 2.5 subevents/log(M_0) for lower magnitudes and 3.3 subevents/log(M_0) for greater magnitude. These earthquakes have a source dimension ~15 km, a typical seismogenic depth of crustal earthquakes (Figure 2a). Large crustal strike-slip earthquake tend to have subvertical faults limited in width by the seismogenic depth and are known for their complex multifault geometry (Kokoxili 2001 (Klinger et al., 2005; Tocheport et al., 2006), Denali 2002 (Eberhart-Phillips et al., 2003), Sumatra 2012 (Meng et al., 2012; Yue et al., 2012), Kaikoura 2016 (Hamling et al., 2017; Wen et al., 2018)). Offshore strike-slip event complexity may be overestimated, however, by contamination of the direct seismic phases with their reverberation in the water column (Yue et al., 2017). Furthermore, among the strike-slip earthquakes of magnitudes greater than M_W6.5, the 267 crustal events (depth lower than 35 km) have a median number of 5 subevents while the 142 deeper events have a median number of 3 subevents.

Large dip-slip earthquakes tend to exhibit less complexity. Their growth in the number of subevents is clearer for moments of $M_0 \geq 6 \times 10^{20}$ ($M_W \approx 7.8$), where the slope becomes 2.5 subevents/log(M_0) if we ignore the M_W9.0 2011 Tohoku earthquake. The M_W 9.0 2011 Tohoku earthquake is an outlier and an extreme case in this regard consistent with rupture of a single, large patch (Ide et al., 2011; Shao et al., 2011). Depth has less influence for $M_W > 6.5$ dip-slip earthquakes since both crustal and deep earthquakes have a median number of subevents of 3.

We find a similar pattern of monotonic growth in the number of subevents in our numerical simulations (Figure 2b). There is a close relationship between prestress variations, and rupture velocity is itself a basic aspect of elastodynamic crack propagation (Eshelby, 1969; Freund, 1998; Kozdon & Dunham, 2013).

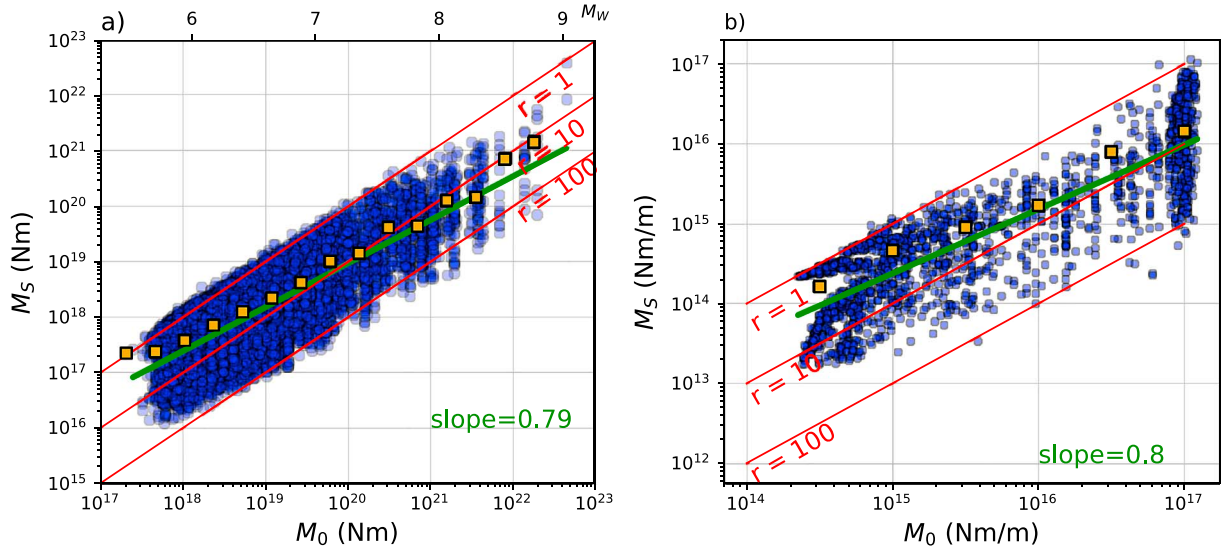

Figure 3. Individual subevent moments plotted against main earthquake moment for observed SCARDEC (a) and modeled (b) STFs. In both figures, blue dots represent a single measurement of subevent/main event pair, orange squares represent the medians over moment bins. The upper horizontal axis in (a) shows the equivalent moment magnitude. Red lines indicate a ratio of seismic moment of subevent to earthquake r of 1, 10, and 100, respectively. The green lines are linear regressions in a log-log space of individual measurements that yield about $M_S \propto M_0^{0.8}$ for the observations (a) and the simulations (b). SCARDEC = Seismic source ChActeristics Retrieved from DEConvolvolving teleseismic body waves; STF = Source Time Function.

Subevents initiate when the rupture front accelerates due to a region of favorable prestress and terminate when the rupture front decelerates due to a region of unfavorable prestress. A more detailed view of the rupture simulations is given in the supporting information (see Figure S8).

3.2. Subevent Scaling

Our second result is that subevent moment is correlated with main event total moment (Figure 3a). To our knowledge, this finding has not previously been reported in the literature. Independent of event magnitude, the ratio of the main event moment to subevent moment is between 1 and 100. The lower bound of this distribution arises from the fact that subevents are rarely found to be larger than the main events, which is true by definition, but the approximation of the Gaussian function to the local moment rate function sometimes brings errors. The upper bound of this distribution arises from the choice of threshold to detect subevents and from ignoring the subevents with duration shorter than 1 s ($4\sigma \geq 1$ s). Of 3,395 STFs, 19 are left out of the analysis with this latter criterion. The scaling remains unchanged by varying the threshold (Figure S2). We see a similar scaling in the USGS data set (Figure S1). Another interesting and supporting aspect is that we did not detect small subevents in the large M_W8+ earthquakes: subevents for such earthquakes are either buried in the signal of the largest subevents and undetectable in our decomposition, or they are absent.

The scaling between subevent moment M_S and main event M_0 for the observed STF is $\log_{10}(M_S) = 0.79\log_{10}(M_0) + 3.22$ and for the simulated STF is $\log_{10}(M_S) = 0.8\log_{10}(M_0) + 2.30$. Our simulations are 2-D, whereas real earthquakes in nature occur on 3-D faults. For this reason, the two scaling relations are not expected to be identical. We are, however, confident that a scaling slope lower than 1, which would support earthquake self-similarity, is a robust feature for both the observed and simulated STFs. It is likely that complexity in the small STFs is underestimated, as discussed in Houston et al. (1998), because the teleseismic data are less reliable at frequencies greater than 1 Hz. Thus, we may not be able to see the smaller and higher frequency subevents. Furthermore, the use of a symmetric Gaussian function for the pulse shape may not be physical (Tinti et al., 2005) as it is intrinsically smoothed. Similar limitations apply to the simulated STF given the low-pass filtering we apply and given the numerical limitations of the experiment.

3.3. Possible Application to Earthquake Early Warning

The correlation between the subevent and main event moment carries potentially a predictive power in estimating the final earthquake moment given observations of the first few subevents. To test this idea, we extract the STF constructed from the 28 September 2018 M_W 7.5 Palu earthquake in Indonesia from the USGS database (https://earthquake.usgs.gov/earthquakes/eventpage/us1000h3p4/finite-fault, last accessed on 19 October 2018; Figure 4). We interpolated the STF with the sampling rate of our previous anal-

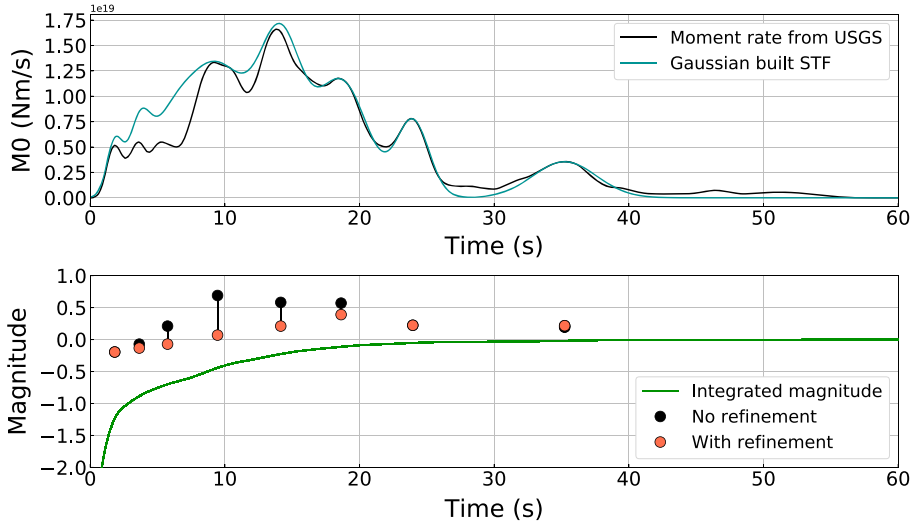

Figure 4. (top) United States Geological Survey (USGS) source time function estimate (https://earthquake.usgs.gov/archive/product/finite-fault/us1000h3p4/us/1539813424642/moment_rate.mr, last accessed on 19 October 2018) in black, linearly interpolated to dt = 0.0703 s, and our Gaussian-built STF in green line. (bottom) "Real time" moment magnitude estimate throughout the rupture: dark green curve is the magnitude difference from the cumulative seismic moment, black dots are the magnitude estimates from individual subevents fitting (using scaling statistics from Figure S3), red dots are the median of all previous magnitude estimates.

ysis. This event was not used in forming the main scaling relation. We begin scanning the STF at the onset of rupture time and we fit the first subevent at t = 1.8 s, which is the time of the first detected peak. At this time we estimate the subevent moment and duration by fitting a Gaussian function (the first half duration and a few samples after its peak), and then apply an algorithm slightly modified from the above described scaling relation to estimate the final event moment (see Text S2).

We find that our algorithm predicts a magnitude of $M_W \approx 7.2$ at ~1.8 s of rupture time, while only $M_W \approx 6.3$ equivalent of moment magnitude was released, and while the final size of the event is $M_W \approx 7.5$ (Figure 4). Upon the second subevent detection at ~3.6 s, which we constrain as being no smaller than 0.25 times the amplitude of the first peak, we calculate an updated moment magnitude estimate and take the mean of both estimates. We iterate as the rupture evolves and refine the magnitude estimates based on the distributions of the previous individual estimates by taking the median value of the peak amplitudes as a threshold of the previous moment magnitude estimates. This allows us to stabilize the magnitude estimates as the variability in subevent size fluctuates during the rupture. An alternative approach to rapid moment estimation based on observing the maximum moment rate (Meier et al., 2017) would require approximately an additional ~10 s of observation beyond that required for our approach.

Earthquake early warning (EEW) systems have latency due to data limitations (proximity of the sensors to the source), due to network delays, and due to methodological errors and uncertainties in interpreting the data. Furthermore, there is not yet an implementation of real-time source time function inversion, which would require an a priori knowledge of the source location and P wave Green's function (the latter can be precomputed and efficiently searched in databases). Goldberg et al. (2018) and Minson et al. (2018) indicate that, at best, magnitude estimates are slightly lower but track the evolution of cumulative moment release (green curve in Figure 4b). The advantage of using the scaling provided described in this paper is therefore a speed up, in the Palu example, of the duration of observation required to produce a final magnitude estimate by about 10 s from current methods.

We have performed a similar exercise as in Figure 4 for the entire SCARDEC database and find that we can predict the final magnitude with a bias of +0.03 and an uncertainty (standard deviation) of 0.52 in moment magnitude within the first 20% of rupture duration (there is a negative bias before 10%, then an overall slight positive bias, see Figure S3b). We find that the largest subevent is detected within 30–50% of the rupture time; however, there are systematic biases, likely due to a structure in the distribution of the subevent size

during the rupture that we have not explored. Nevertheless, these biases may be accounted for in a future improvement and application of this scaling.

4. Discussion and Conclusions

Through an analysis of earthquake STFs and their subevents, we make several observations. First, large earthquakes have more subevents than small earthquakes, contradicting the idea of self-similarity in earthquakes (Allmann & Shearer, 2009; Prieto et al., 2004) but agreeing with several previous and local observations (Ellsworth & Beroza, 1998; Sato & Mori, 2006). Second, the subevent moment scales with the main event moment with a power exponent of about 0.8.

We find that simulations with spatially uniform fault parameters fail to produce subevents but that introducing a range of heterogeneity levels in the prestress yields similar results. We conclude that we were unable to constrain the strength of fault heterogeneity from the subevent scaling. Instead, we simply make the weaker claim that the heterogeneous prestress distributions we analyze are consistent with the observations.

Because both simple simulations and observations share similar statistical properties of subevent-to-main event moment, we conclude that the dynamics of rupture, with the physics tested in our simulations, exhibits a sense of self-organization such that the complexity of earthquakes is structured; the subevents have neither a fixed nor a random size. We propose that the same variations in fault prestress that create subevents in STFs also give rise to the scaling between subevent moment and main event moment. Main event-subevent scaling then occurs because a favorably prestressed region creates a large subevent that is more likely to rupture through a surrounding unfavorably prestressed region (Eshelby, 1969; Kozdon & Dunham, 2013). It is in this way that a large subevent is more likely to be part of a large total rupture rather than a small one.

We have shown that the statistical properties of the subevent moment relative to the main event moment may be utilized for early magnitude estimates. Our results do not imply that earthquakes are deterministic in the sense that early nucleation is indicative of the entire evolution of rupture (Beroza & Ellsworth, 1996; Goldberg et al., 2018; Iio, 1995; Meier et al., 2017; Melgar & Hayes, 2017), but rather that we can exploit the patterns in earthquake complexity to statistically infer the future number and size of subevents from the first subevent. Our results are mostly practical for strike-slip events that tend to have shorter duration subevents. Using STFs for early warning is not yet in place as the latency of current EEW systems delay magnitude estimates. Rapid STF estimation for EEW could be possible pending further investigation.

The caveats of this study are mainly the frequency bandwidth limitations for small events. Furthermore, the attenuation models used in SCARDEC and USGS databases are globally averaged, yielding inaccuracies in regions that have abnormally strong or weak seismic attenuation. Our results are nevertheless robust for magnitudes 7 and greater.

Acknowledgments
This research was supported by the Southern California Earthquake Center (SCEC) award 17001, under National Science Foundation Cooperative agreement EAR-1033462 and U.S. Geological Survey Cooperative agreement G12AC20038. The SCEC contribution number of this paper is 8978. The following are the authors' contributions: P. D. designed the subevent decomposition, performed the observations, analysis, made versions of the figures, and wrote the original draft. J. Y. performed the simulation analysis and helped in editing the manuscript. B. P. L. provided guidance with the numerical simulations, mechanical analysis, and helped write and revise the manuscript. M. D. designed and managed the project, served an advisory role to J. Y. and P. D., and edited the manuscript and figures. None of the authors have any conflict or competing interest. The SCARDEC database is open to the public http://scardec.projects.sismo.ipgp.fr/ and the SBIEMLAB codes are maintained by J. P. Ampuero at http://web.gps.caltech.edu/~ampuero/software.html. All scripts and samples of data are available at github.com/mdenolle/subevents2019/.

References

Allen, R. M., & Kanamori, H. (2003). The potential for earthquake early warning in Southern California. *Science*, *300*(5620), 786–789. https://doi.org/10.1126/science.1080912

Allen, R. M., & Melgar, D. (2019). Earthquake early warning: Advances, scientific challenges, and societal needs. *Annual Review of Earth and Planetary Sciences*, *47*, 361–388. https://doi.org/10.1146/annurev-earth-053018-060457

Allmann, B. P., & Shearer, P. M. (2009). Global variations of stress drop for moderate to large earthquakes. *Journal of Geophysical Research*, *114*, B01310. https://doi.org/10.1029/2008JB005821

Ando, R., & Kaneko, Y. (2018). Dynamic rupture simulation reproduces spontaneous multifault rupture and arrest during the 2016 M_w 7.9 Kaikoura earthquake. *Geophysical Research Letters*, *45*, 12,875–12,883. https://doi.org/10.1029/2018GL080550

Beroza, G. C., & Ellsworth, W. L. (1996). Properties of the seismic nucleation phase. *Tectonophysics*, *261*, 209–227. https://doi.org/10.1016/0040-1951(96)00067-4

Boatwright, J. (1984). The effect of rupture complexity on estimates of source size. *Journal of Geophysical Research*, *89*, 1132–1146. https://doi.org/10.1029/JB089iB02p01132

Chounet, A., & Vallée, M. (2018). Global and interregion characterization of subduction interface earthquakes derived from source time functions properties. *Journal of Geophysical Research: Solid Earth*, *123*, 5831–5852. https://doi.org/10.1029/2018JB015932

Chounet, A., Vallée, M., Causse, M., & Courboulex, F. (2018). Global catalog of earthquake rupture velocities shows anticorrelation between stress drop and rupture velocity. *Tectonophysics*, *733*, 148–158. https://doi.org/10.1016/j.tecto.2017.11.005

Colombelli, S., Zollo, A., Festa, G., & Picozzi M. (2014). Evidence for a difference in rupture initiation between small and large earthquakes. *Nature Communications*, *5*, 3958. https://doi.org/10.1038/ncomms4958

Denolle, M. A. (2019). Energetic onset of earthquakes. *Geophysical Research Letters*, *46*, 2458–2466. https://doi.org/10.1029/2018GL080687

Dunham, E. M., Belanger, D., Cong, L., & Kozdon, J. E. (2011). Earthquake ruptures with strongly rate-weakening friction and off-fault plasticity, Part 2: Nonplanar faults. *Bulletin of the Seismological Society of America*, *101*, 2308–2322. https://doi.org/10.1785/0120100076

Eberhart-Phillips, D., Peter J. Haeussler, Freymueller, J. T., Frankel, A. D., Rubin, C. M., Craw, P., et al. (2003). The 2002 Denali fault earthquake, Alaska: A large magnitude, slip-partitioned event. *Science*, *300*, 1113–1118. https://doi.org/10.1126/science.1082703

Ellsworth, W. L., & Beroza, G. C. (1998). Observation of the seismic nucleation phase in the Ridgecrest, California, earthquake sequence. *Geophysical research letters*, *25*, 401–404.

Eshelby, J. (1969). The elastic field of a crack extending non-uniformly under general anti-plane loading. *Journal of the Mechanics and Physics of Solids*, *17*, 177–199.

Fang, Z., & Dunham, E. M. (2013). Additional shear resistance from fault roughness and stress levels on geometrically complex faults. *Journal of Geophysical Research: Solid Earth*, *118*, 3642–3654. https://doi.org/10.1002/jgrb.50262

Freund, L. B. (1998). *Dynamic fracture mechanics*. Cambridge University Press.

Goldberg, D. E., Melgar, D., Bock, Y., & Allen, R. M. (2018). Geodetic observations of weak determinism in rupture evolution of large earthquakes. *Journal of Geophysical Research: Solid Earth*, *123*, 9950–9962. https://doi.org/10.1029/2018JB015962

Hamling, I. J., Hreinsdóttir, S., Clark, K., Elliott, J., Liang, C., Fielding, E., et al. (2017). Complex multifault rupture during the 2016 M_w 7.8 Kaikōura earthquake, New zealand. *Science*, *356*, 6334–7194. https:/doi.org/10.1126/science.aam7194

Hayes, G. P. (2017). The finite, kinematic rupture properties of great-sized earthquakes since 1990. *Earth and Planetary Science Letters*, *468*, 94–100. https://doi.org/10.1016/j.epsl.2017.04.003

Houston, H. (2001). Influence of depth, focal mechanism, and tectonic setting on the shape and duration of earthquake source time functions. *Journal of Geophysical Research*, *106*, 11,137–11,150. https://doi.org/10.1029/2000JB900468

Houston, H., Benz, H. M., & Vidale, J. E. (1998). Time functions of deep earthquakes from broadband and short-period stacks. *Journal of Geophysical Research*, *103*, 29,895–29,913.

Huang, Y., Meng, L., & Ampuero, J.-P. (2012). A dynamic model of the frequency-dependent rupture process of the 2011 Tohoku-Oki earthquake. *Earth, planets and space*, *64*, 1061–1066. https://doi.org/10.5047/eps.2012.05.011

Ide, S., & Aochi, H. (2005). Earthquakes as multiscale dynamic ruptures with heterogeneous fracture surface energy. *Journal of Geophysical Research*, *110*, B11303. https://doi.org/10.1029/2004JB003591

Ide, S., Baltay, A., & Beroza, G. C. (2011). Shallow dynamic overshoot and energetic deep rupture in the 2011 M_w 9.0 Tohoku-Oki earthquake. *Science*, *332*, 1426–1429. https://doi.org/10.1126/science.1207020

Iio, Y. (1995). Observations of the slow initial phase generated by microearthquakes: Implications for earthquake nucleation and propagation. *Journal of Geophysical Research*, *100*, 15,333–15,349.

Ji, C., Wald, D. J., & Helmberger, D. V. (2002). Source description of the 1999 Hector Mine, California, earthquake, Part I: Wavelet domain inversion theory and resolution analysis. *Bulletin of the Seismological Society of America*, *92*, 1192–1207. https://doi.org/10.1785/0120000916

Kikuchi, M., & Kanamori, H. (1982). Inversion of complex body waves. *Bulletin of the Seismological Society of America*, *72*, 491–506.

Kikuchi, M., & Kanamori, H. (1991). Inversion of complex body waves—III. *Bulletin of the Seismological Society of America*, *81*, 2335–2350.

Klinger, Y., Xu, X., Tapponnier, P., der Woerd, J. V., Lasserre, C., & King, G. (2005). High-resolution satellite imagery mapping of the surface rupture and slip distribution of the M_w, 7.8, 14 November 2001 Kokoxili earthquake, Kunlun fault, Northern Tibet, China. *Bulletin of the Seismological Society of America*, *95*, 1970–1987. https://doi.org/10.1785/0120040233

Kozdon, J. E., & Dunham, E. M. (2013). Rupture to the trench: Dynamic rupture simulations of the 11 March 2011 Tohoku earthquake. *Bulletin of the Seismological Society of America*, *103*, 1275–1289. https://doi.org/10.1785/0120120136

Meier, M.-A., Ampuero, J. P., & Heaton, T. H. (2017). The hidden simplicity of subduction megathrust earthquakes. *Science*, *357*, 1277–1281. https://doi.org/10.1126/science.aan5643

Melgar, D., & Hayes, G. P. (2017). Systematic observations of the slip pulse properties of large earthquake ruptures. *Geophysical Research Letters*, *44*, 9691–9698. https://doi.org/10.1002/2017GL074916

Meng, L., Ampuero, J.-P., Stock, J., Duputel, Z., Luo, Y., & Tsai, V. C. (2012). Earthquake in a maze: Compressional rupture branching during the 2012 M_w 8.6 Sumatra earthquake. *Science*, *337*, 724–726. https://doi.org/10.1126/science.1224030

Minson, S. E., Meier, M.-A., Baltay, A. S., Hanks, T. C., & Cochran, E. S. (2018). The limits of earthquake early warning: Timeliness of ground motion estimates. *Science Advances*, *4*. https://doi.org/10.1126/sciadv.aaq0504

Mueller, C. S. (1985). Source pulse enhancement by deconvolution of an empirical Green's function. *Geophysical Research Letters*, *12*, 33–36.

Noda, S., & Ellsworth, W. L. (2016). Scaling relation between earthquake magnitude and the departure time from *p* wave similar growth. *Geophysical Research Letters*, *43*, 9053–9060. https://doi.org/10.1002/2016GL070069

Olson, E. L., & Allen, R. M. (2005). The deterministic nature of earthquake rupture. *Nature*, *438*, 212. https://doi.org/10.1038/nature04214

Prieto, G. A., Shearer, P. M., Vernon, F. L., & Kilb, D. (2004). Earthquake source scaling and self-similarity estimation from stacking *p* and *s* spectra. *Journal of Geophysical Research*, *109*, B08310. https://doi.org/10.1029/2004JB003084

Ripperger, J., Ampuero, J.-P., Mai, P. M., & Giardini, D. (2007). Earthquake source characteristics from dynamic rupture with constrained stochastic fault stress. *Journal of Geophysical Research*, *112*, B04311. https://doi.org/10.1029/2006JB004515

Sato, K., & Mori, J. (2006). Relationship between rupture process complexity and earthquake size. *Journal of Geophysical Research*, *111*, B05307. https://doi.org/10.1029/2005JB003614

Shao, G., Ji, C., & Zhao, D. (2011). Rupture process of the 9 March, 2011 M_w 7.4 sanriku-oki, Japan earthquake constrained by jointly inverting teleseismic waveforms, strong motion data and gps observations. *Geophysical Research Letters*, *38*, L00G20. https://doi.org/10.1029/2011GL049164

Shearer, P. M., Prieto, G. A., & Hauksson, E. (2006). Comprehensive analysis of earthquake source spectra in Southern California. *Journal of Geophysical Research*, *111*, B06303. https://doi.org/10.1029/2005JB003979

Stork, A., & Ito, H. (2004). Source parameter scaling for small earthquakes observed at the western Nagano 800-m-deep borehole, central Japan. *Bulletin of the Seismological Society of America*, *94*, 1781–1794. https://doi.org/10.1785/012002214

Tanioka, Y., & Ruff, L. J. (1997). Source time functions. *Seismological Research Letters*, *68*, 386. https://doi.org/10.1785/gssrl.68.3.386

Tinti, E., Fukuyama, E., Piatanesi, A., & Cocco, M. (2005). A kinematic source-time function compatible with earthquake dynamics. *Bulletin of the Seismological Society of America*, *95*, 1211. https://doi.org/10.1785/0120040177

Tocheport, A., Rivera, L., & der Woerd, J. V. (2006). A study of the 14 November 2001 Kokoxili earthquake: History and geometry of the rupture from teleseismic data and field observations. *Bulletin of the Seismological Society of America*, *96*, 1729–1741. https://doi.org/10.1785/0120050200

Vallée, M. (2013). Source time function properties indicate a strain drop independent of earthquake depth and magnitude. *Nature Communications*, *4*, 2606. https://doi.org/10.1038/ncomms3606

Vallée, M., Ampuero, J. P., Juhel, K., Bernard, P., Montagner, J.-P., & Barsuglia, M. (2017). Observations and modeling of the elastogravity signals preceding direct seismic waves. *Science*, *358*, 1164–1168. https://doi.org/10.1126/science.aao0746

Vallée, M., & Douet, V. (2016). A new database of source time functions (STFs) extracted from the SCARDEC method. *Physics of the Earth and Planetary Interiors*, *257*, 149–157. https://doi.org/10.1016/j.pepi.2016.05.012

Vallée, M., & Juhel, K. (2019). Multiple observations of the prompt elastogravity signals heralding direct seismic waves. *Journal of Geophysical Research: Solid Earth*, *124*, 2970–2989. https://doi.org/10.1029/2018JB017130

Wen, Y.-Y., Ma, K.-F., & Fry, B. (2018). *Multiple-fault, slow rupture of the 2016* M_W *7.8 Kaikōura, New Zealand Earthquake*. Complementary insights from teleseismic and geodetic data: Bulletin of the Seismological Society of America. https://doi.org/10.1785/0120170285

Wu, Y.-M., Yi, H., Zhao, L., Huang, B. S., & Liang W. T. (2006). Magnitude determination using initial *p* waves: A single-station approach. *Geophysical Research Letters*, *33*, L05306. https://doi.org/10.1029/2005GL025395

Ye, L., Lay, T., Kanamori, H., & Rivera, L. (2016). Rupture characteristics of major and great ($M_w \geq 7.0$) megathrust earthquakes from 1990 to 2015: 1. Source parameter scaling relationships. *Journal of Geophysical Research: Solid Earth*, *121*, 826–844. https://doi.org/10.1002/2015JB012426

Yue, H., Castellanos, J., Yu, C., Meng, L., & Zhan, Z. (2017). Localized water reverberation phases and its impact on backprojection images. *Geophysical Research Letters*, *44*, 9573–9580. https://doi.org/10.1002/2017GL073254

Yue, H., Lay, T., & Koper, K. D. (2012). En échelon and orthogonal fault ruptures of the 11 April 2012 great intraplate earthquakes. *Nature*, *490*, 245. https://doi.org/10.1038/nature11492

Zhan, Z., Kanamori, H., Tsai, V. C., Helmberger, D. V., & Wei, S. (2014). Rupture complexity of the 1994 Bolivia and 2013 Sea of Okhotsk Deep earthquakes. *Earth and Planetary Science Letters*, *385*, 89–96. https://doi.org/10.1016/j.epsl.2013.10.028